Observations and Theory of the AMPTE Magnetotail Barium Releases

P. A. BERNHARDT, R. A. ROUSSEL-DUPRE, AND M. B. PONGRATZ

Los Alamos National Laboratory, Los Alamos, New Mexico

G. HAERENDEL AND A. VALENZUELA

Max-Planck-Institut für Physik und Astrophysik, Garching bei München, Federal Republic of Germany

D. A. GURNETT AND R. R. ANDERSON

Department of Physics and Astronomy, University of Iowa, Iowa City

The barium releases in the magnetotail during the Active Magnetospheric Particle Tracer Explorers (AMPTE) operation were monitored by ground-based imagers and by instruments on the Ion Release Module. After each release, the data show the formation of a structured diamagnetic cavity. The cavity grows until the dynamic pressure of the expanding ions balances the magnetic pressure on its surface. The magnetic field inside the cavity is zero. The barium ions collect on the surface of the cavity, producing a shell. Plasma irregularities form along magnetic field lines draped over the surface of the cavity. The scale size of the irregularities is nearly equal to the thickness of the shell. The evolution and structuring of the diamagnetic cavity are modeled using magnetohydrodynamics theory.

1. EXPERIMENT SUMMARY

During the Active Magnetospheric Particle Tracer Explorers (AMPTE) campaign, two barium releases in the magnetotail produced diamagnetic cavities. The injected neutral barium atoms expanded radially and were photoionized with a time constant of 28 s. The barium ions continued to expand radially, but the photoelectrons were produced with a random velocity corresponding to 0.7 eV. The time and distance scales for the magnetotail releases are given in Table 1.

The electron and ion cyclotron frequencies are given as $\Omega_{ce} = eB/m_e$ and $\Omega_{ci} = eB/m_i$. The ion velocity is the initial radial velocity of the barium release. The electron velocity is computed assuming that $\beta = 1$ at the cloud surface. The plasma densities are based on in situ measurements from the AMPTE Ion Release Module (IRM) and from calibrated images of the fluorescent barium ions. The ion and electron Larmor radii are $r_{Li} = v_i/\Omega_{ci}$ and $r_{Le} = v_e/\Omega_{ce}$, respectively.

The ion gyroradius was much larger than the electron gyroradius. The electrons tended to become attached to the magnetic field lines while the ions moved radially with only slight bending of their trajectories. Consequently, an electric field, pointing radially inward, was produced by the charge separation. The electrons drifted in the $\mathbf{E} \times \mathbf{B}$ direction where $\mathbf{E}$ is the polarization electric field and $\mathbf{B}$ is the ambient uniform magnetic field. The $\mathbf{E} \times \mathbf{B}$ drift and the diamagnetic drift associated with the density gradient of the surface of the cloud contributed to currents at the surface of the cloud. These currents $\mathbf{j}$ formed loops around the surface of the expanding ion cloud in planes perpendicular to the ambient magnetic field. The currents increased until the magnetic field inside the cavity vanished and the internal electrons were no longer magnetized, allowing them to move radially outward in response to the electric field. By this process the plasma formed

into a layer at the surface of the diamagnetic cavity. A $\mathbf{j} \times \mathbf{b}$ force inhibited the expansion of the cavity, causing an eventual collapse. The theory of the formation and collapse of the diamagnetic cavity is presented in sections 2, 3, and 4.

The barium ion cloud did not expand as a smooth shell. Irregularities, aligned with the disturbed magnetic field, formed on the surface. Fluid or kinetic instabilities provided the irregularities. One candidate mechanism for this process is the lower hybrid drift (LHD) instability. Cross-field currents in conjunction with density and magnetic field gradients can excite this instability, producing field-aligned irregularities with perpendicular wave numbers of the order of an inverse electron gyroradius. The irregularity wavelength computed for the March 21, 1985, event is 3 km, whereas the measured wavelength is 40 km. Similar results are also seen in the May 13, 1985, data.

The irregularity scale size seems to be the same as the thickness of the shell at the surface of the cloud. A fluid interchange instability that produces flute irregularities with the appropriate scale is described in section 5.

2. OBSERVATIONS

A large network of optical stations was established by the Max-Planck-Institut (MPI) for observations of all the AMPTE releases. Release location predictions were distributed to the observing stations by MPI. The decision for release was partially based on the viewing conditions at the ground optical sites.

The data presented in this report were obtained at the Ortho site located on the southern end of the White Sands Missile Range (WSMR) and at Breezy Point near the Los Alamos National Laboratory. Other data from the Massachusetts Institute of Technology/Lincoln Laboratory (MIT/LL) Experimental Test Site (ETS) and from the Air Force Maui Optical Station (AMOS) showed similar results and could be used for triangulation in future studies. The locations of the four observation stations are given in Table 2.

TABLE 1. AMPTE Magnetotail Release Parameters

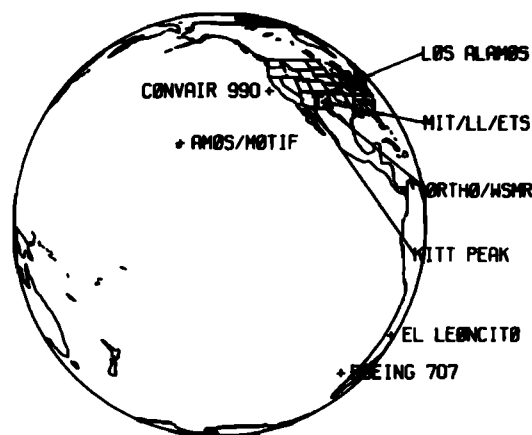|	Release Date, UT	
	March 21, 0920:38	May 13, 0517:13
Magnetic field, nT	8.0	17.6
B_x, B_y, B_z, nT	−7.5, 2, 2	−14, 7, 8
Ω_{ci}, s^{-1}	5.2×10^{-3}	11.1×10^{-3}
Ω_{ce}, s^{-1}	1.4×10^3	3.1×10^3
$n_e = n_i$ (barium plasma), cm^{-3}	240	1100
$n_e = n_i$ (background plasma), cm^{-3}	0.9	0.2
v_b, m/s	1.3×10^3	1.3×10^3
v_e, m/s	5.0×10^5	5.0×10^5
r_{Li}, m	2.1×10^5	1.0×10^5
r_{Le}, m	360	160
Kp (magnetic disturbance index)	0	4
T_e (background), K	5×10^6	1.3×10^7
T_i (background), K	3×10^7	6.0×10^7

Fig. 1. Optical sites deployed to make observations of the March 21, 1985, barium release in the magnetotail. The earth is observed from the release point.

The data reported here are a subset of the total data collected. Images from an intensified film camera at Breezy Point and a charge coupled device (CCD) camera at Ortho are described in detail later. All images are oriented so that the earth's equatorial plane is horizontal.

The intensified film camera used a 400-mm focal length lens with a 200-mm aperture. The image was filtered at 455.4 nm, a barium ion emission line. A 25-mm-diameter microchannel plate intensifier provided light gain of 5000. An 85-mm, $f/1.0$ relay lens transferred the image from the intensifier to 35-mm TRI-X film.

The intensified CCD camera used a 2500-mm focal length Cassegrain lens with 800-mm aperture. After passing through a 455.4-nm interference filter, the barium ion cloud images were focused on a 40-mm microchannel plate intensifier. A 50-mm, $f/1.2$ relay lens focused the intensified image on a 512×320 pixel array. Each pixel in the CCD array was digitized to 14 bits and stored on magnetic tape. The CCD camera is operated by a 68000 microprocessor. Postexperimental data analysis uses the computer and associated 1.25 megabytes of memory.

The first magnetotail release of barium occurred on March 21, 1985. The ground observation stations from the point of view of the release are illustrated in Figure 1. The event occurred during quiet time periods when the Kp index was zero.

The photometer observed emissions from neutral barium at 553.5-nm wavelength for the March 21, 1985, release. The light intensity was converted into apparent neutral barium inventory using a conversion factor of 3.02×10^{-18} W/atom [Horak and Whitaker, 1982]. The converted photometer record is illustrated by the solid curve in Figure 2. Because the neutral barium cloud is initially optically thick, the record for

the first 90 s did not represent the total cloud inventory. The initial cloud inventory is estimated with the dashed curve in Figure 2. This curve uses a decay time of 28 s, which is the photoionization rate of neutral barium in full sunlight [Carlsten, 1975]. The photometer data are not accurate enough to improve the accuracy of the photoionization rate. The data, however, are consistent with a value of 28 s. The analysis yields 7.5×10^{24} particles for the initial amount of barium released. This quantity is used as an input for our theoretical models.

The images from the intensified film camera operated on March 21, 1985, are shown in Figures 3 and 4. The set of 2-s exposures in Figure 3 shows the expansion of the ion cloud. The radial expansion speed is 1.3 km/s. The sequence of pictures shows the formation and collapse of the diamagnetic cavity.

The 16-s exposures of Figure 4 illustrate a plasma jet on the left side of the cloud at 0922:08 and a "halo" of plasma in the times from 0926:08 through 0941:11. These ions were not captured by the collapsing diamagnetic cavity. They may have escaped the cavity on large gyroradius orbits or through some instability process as indicated by the field-aligned structure.

The CCD images from Ortho are higher resolution than the film images. Figure 5 shows the formation of the diamagnetic

TABLE 2. AMPTE Magnetotail Release Observation Stations Sponsored by Los Alamos

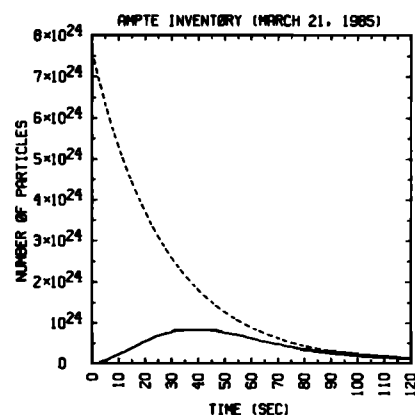| Name	Latitude, °N	Longitude, °E	Altitude, km
Los Alamos (Breezy Point)	35.772	−106.253	1.957
MIT/LL/ETS	33.817	−106.699	1.532
Ortho/WSMR	32.467	−106.275	1.218
AMOS	20.708	−156.258	3.049

Fig. 2. Photometer measurement of neutral barium inventory using 553.5-nm line emissions. Dashed line is estimate of measurement if the barium cloud were optically thin.
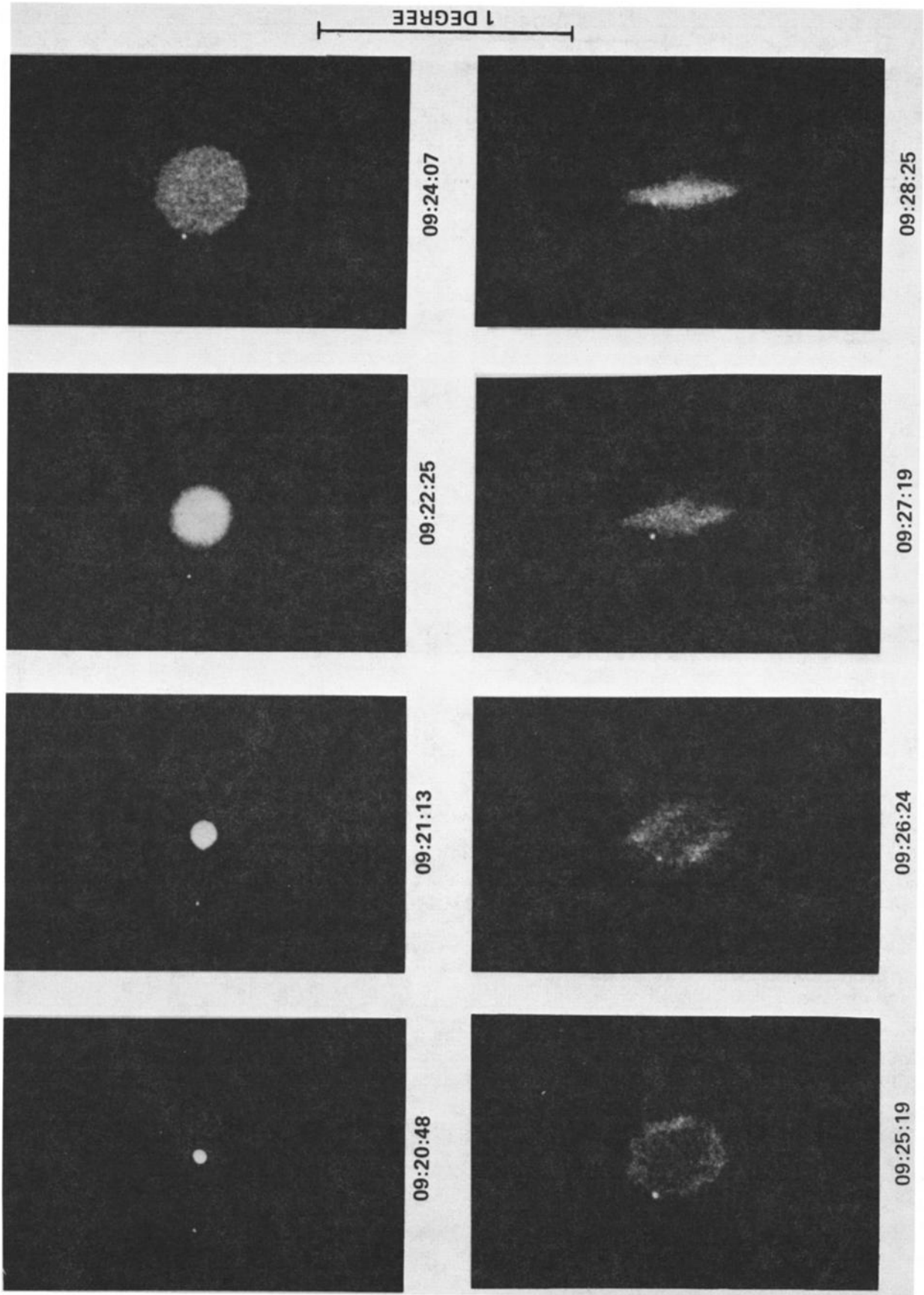
Fig. 3. Sequence of 2-s exposures of the AMPTE barium release in the magnetotail, March 21, 1985, from the intensified film camera operated at the Los Alamos Mobile Optical Tracker (LAMOT) station set up at Breezy Point. Times are in universal time.
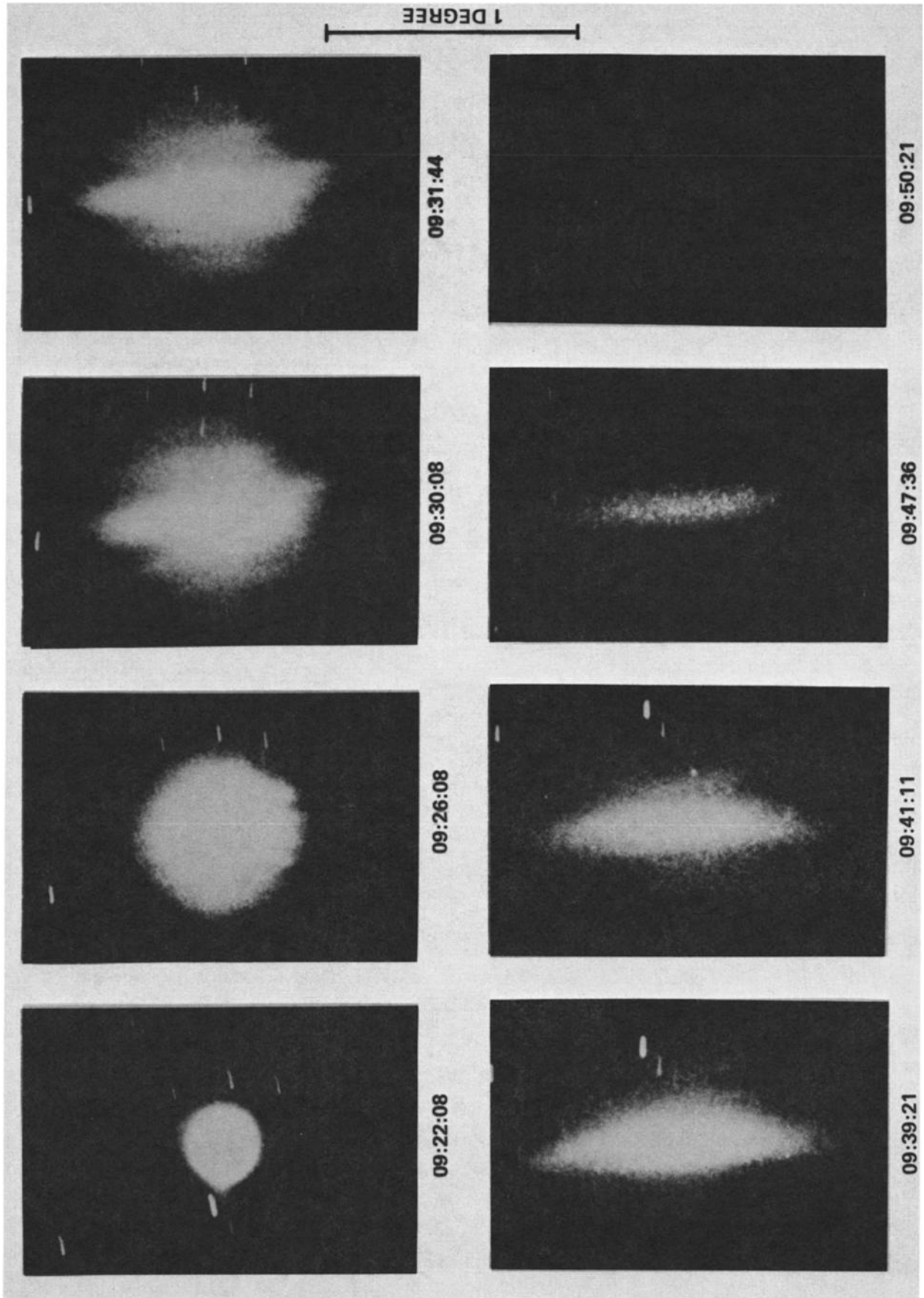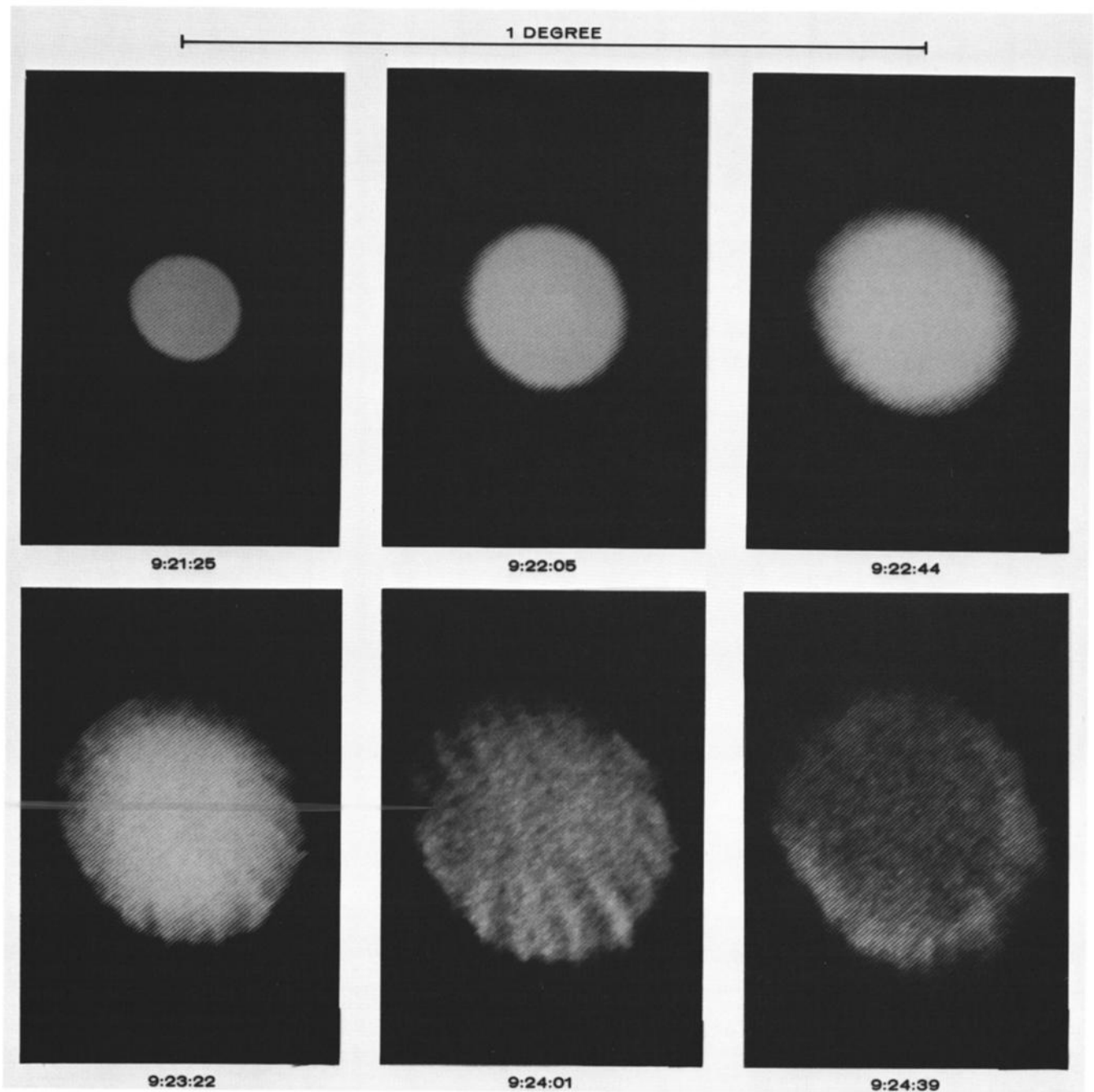
Fig. 4. Sequence of 16-s exposures obtained by the LAMOT.

Fig. 5. Sequence of 2-s exposures obtained from the CCD imager operated at the Ortho site on the White Sands Missile Range, New Mexico. A diamagnetic cavity forms in the weak magnetic field.

cavity. The surface of the cavity becomes draped with irregularities aligned with the perturbed magnetic field.

Figure 6 illustrates the collapse of the cavity and the motion of the surface irregularities. After the collapse the ion cloud slowly convected away from the IRM in the low Kp environment (Figure 7).

The position of the AMPTE ion cloud is plotted in celestial coordinates in Figure 8. The cloud drifts along the IRM trajectory (dashed line) for 400 s. Motion away from the trajectory at 400 m/s occurs after the cavity has collapsed and the ions are captured by the flow of the ambient medium.

The CCD images have been scanned and calibrated to yield the ion content profiles illustrated in Figure 9. The background has been subtracted, but the data points have not been smoothed. The slices are made at 45° to the images in Figures 5, 6, and 7. Negative distances are at the lower left part of the images. The central reduction in ion content at 0922:05 appears because the barium is released as an expanding spherical surface. One side of the diamagnetic cavity is steeper than the other side at 0924:01. The ion content of the cavity is uniform until 0924:39, when the ions begin to collect on the surface. This surface structure lasts until the termination of the collapse.

A smoothed radial profile 87 s after release is shown in the left panel of Figure 10. These data are used to determine a profile for the initial velocity distribution (Figure 10, right panel). This distribution is normalized so that integration over velocity space yields unity. The cloud expands with a characteristic velocity of 1300 m/s.

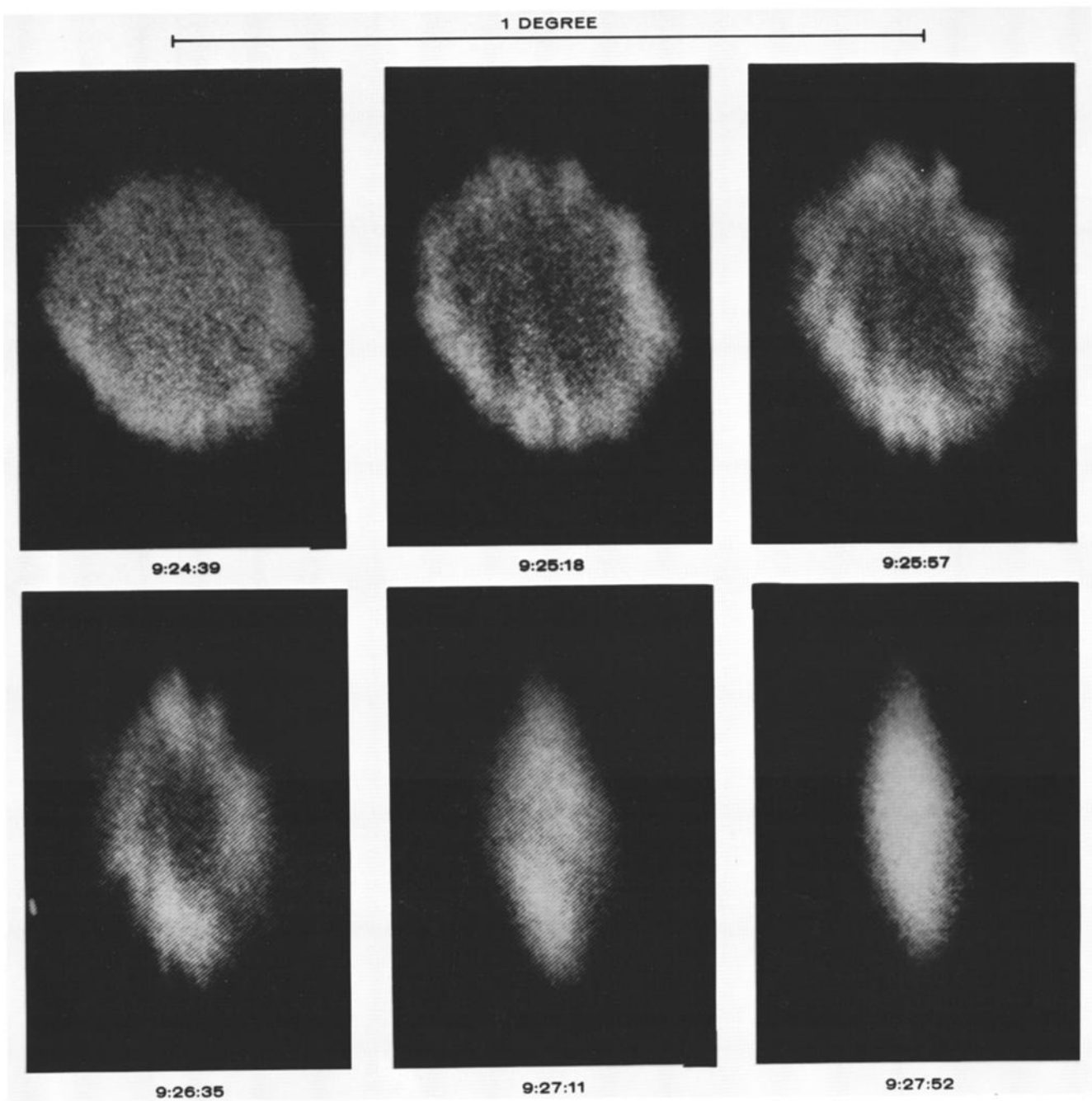The ion density profile is shown in Figure 11, 87 s after

1 DEGREE

Fig. 6.   Sequence of 2-s exposures from Ortho showing the collapse of the cavity.

release. Integration over space gives 7.5×10^{24} particles. The central density is 490 cm^{-3}. The maximum density of the shell is 880 cm^{-3}. The in situ measurements by the plasma wave observations of the AMPTE IRM spacecraft also reveal a shell-like density distribution [*Gurnett et al.*, 1986]. The frequency-time spectrogram from the March 21 event shows (1) electron plasma oscillations from the central density of the cloud and (2) propagation cutoff by the peak density of the shell (Figure 12 top). The densities obtained from the optical observations and from the in situ wave data agree within a factor of 2.

The sudden increase in electron density at 0927 is coincident with the final stage in the collapse of the cloud as seen in the optical images (Figure 6, last image). The subsequent reduction in electron density is a result of the convection of the ion cloud from the IRM trajectory (Figure 8).

The bottom graph in Figure 12 illustrates the magnetic field fluctuations associated with the diamagnetic cavity. The magnetic flux density inside the cavity is zero. The magnetic field returns to a near-normal value only after the cavity has collapsed. Further details on the in situ magnetic field measurements are given by *Lühr et al.* [1986].

A color-encoded set of CCD images is shown in Plate 1. The colors indicate the column density of barium ions. After the collapse the maximum ion content at 0927:52 returns to the precollapse value at 0923:22.

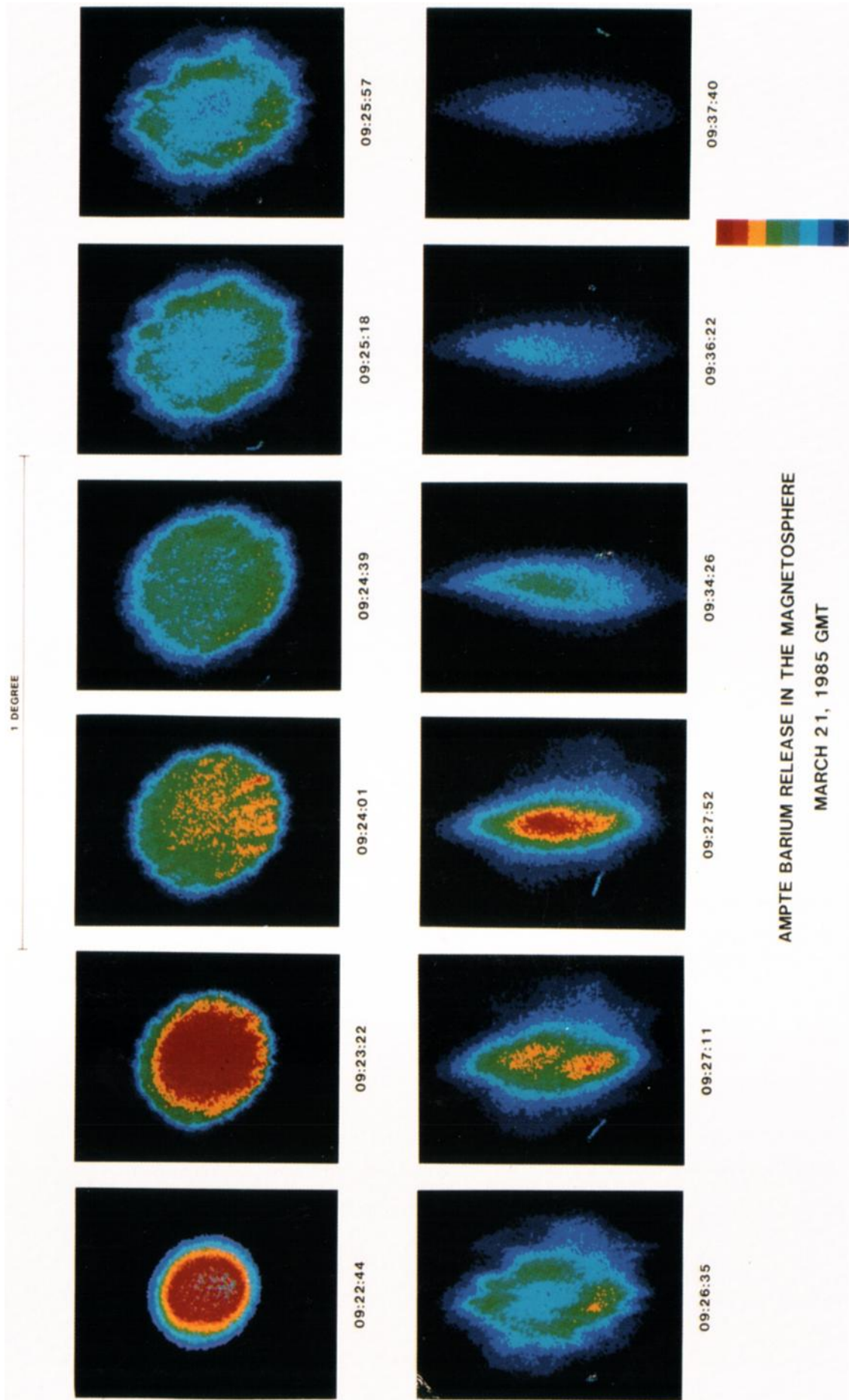The combination of ground-based optical data and in situ IRM measurements gives a complete picture of the barium

AMPTE BARIUM RELEASE IN THE MAGNETOSPHERE
MARCH 21, 1985 GMT

Plate 1. Color contours of CCD images taken from Ortho. The color bar represents uniform steps of 10^9 cm^{-2} from 7×10^9 cm^{-2} (red) to zero (black). Substantial intensity increase occurs after collapse of the diamagnetic cavity.
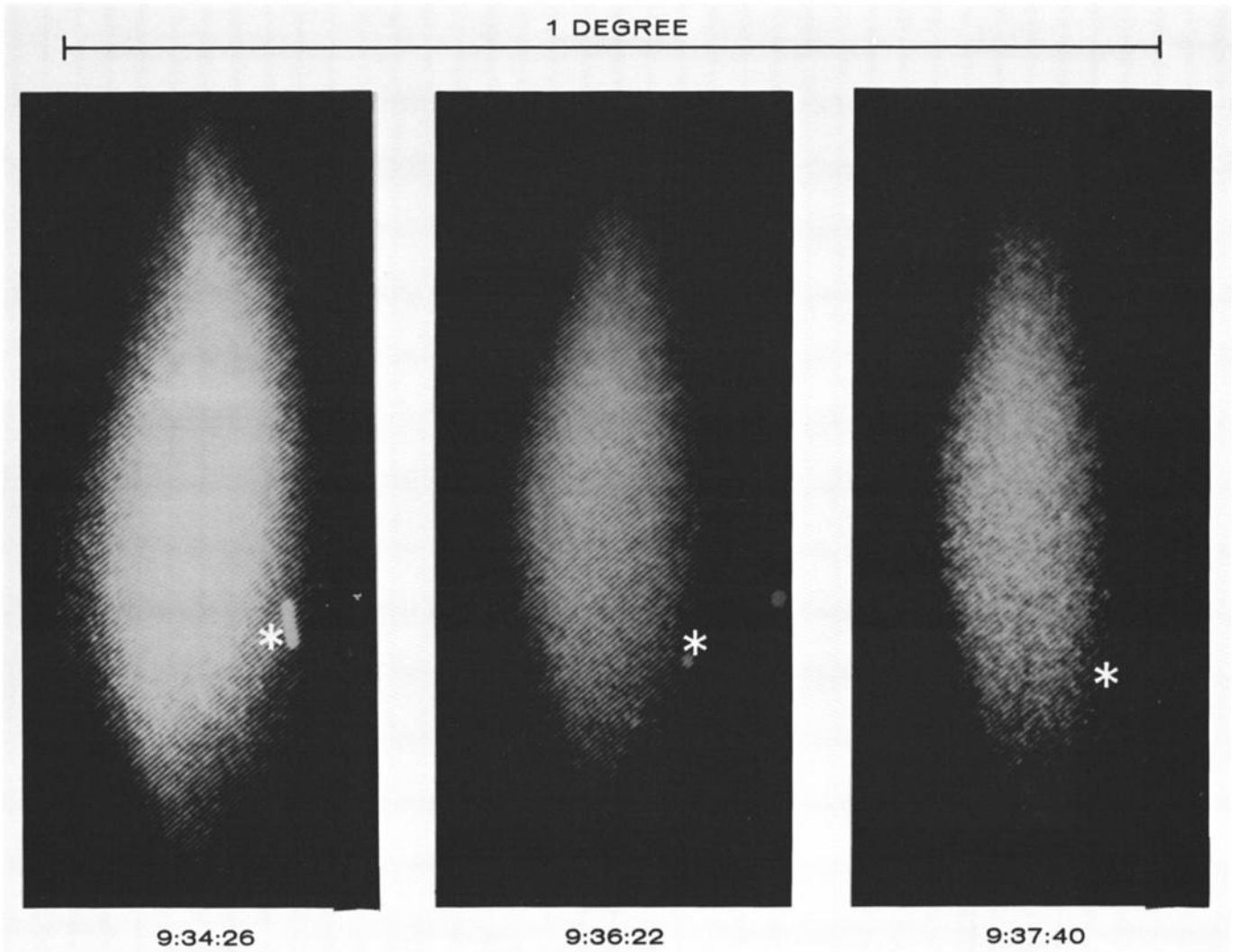
Fig. 7.   Measurements from Ortho of the ion cloud images drifting away from the Ion Release Module (asterisks).

release in the magnetotail. Detailed theoretical analysis of the data has been applied to the formation, collapse, and structuring of the diamagnetic cavity. This is discussed in the subsequent sections.

3. BASIC PLASMA PHYSICS

To study the magnetic cavity, we model the expanding cloud as a conducting shell with zero internal magnetic field. In spherical polar coordinates, variations occur in the radial (r), meridional (θ), and azimuthal (ϕ) directions. All of the mass in the plasma is taken to lie on a surface, given by

$$r = D(\theta, \phi, t) \qquad (1)$$

where D is a function defining the radial distance to the cavity boundary. The mass density is

$$\rho(r, \theta, \phi, t) = mn(\theta, \phi, t)\delta[r - D(\theta, \phi, t)] \qquad (2)$$

where m is the ion mass, $n(\theta, \phi, t)$ is the integrated number density across the shell, and $\delta(\ )$ is the Dirac delta function. The radial, meridional, and azimuthal components of the shell velocity are $v_r(\theta, \phi, t)$, $v_\theta(\theta, \phi, t)$, and $v_\phi(\theta, \phi, t)$, respectively.
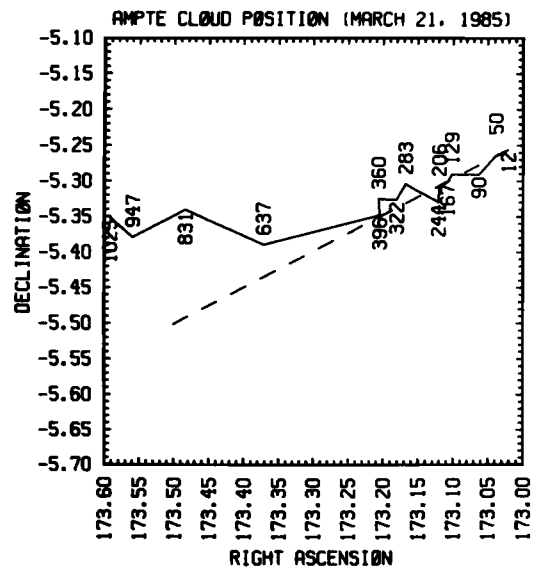

Fig. 8.   Ion cloud position (solid line) and IRM position (dashed line) obtained from CCD images taken at Ortho.
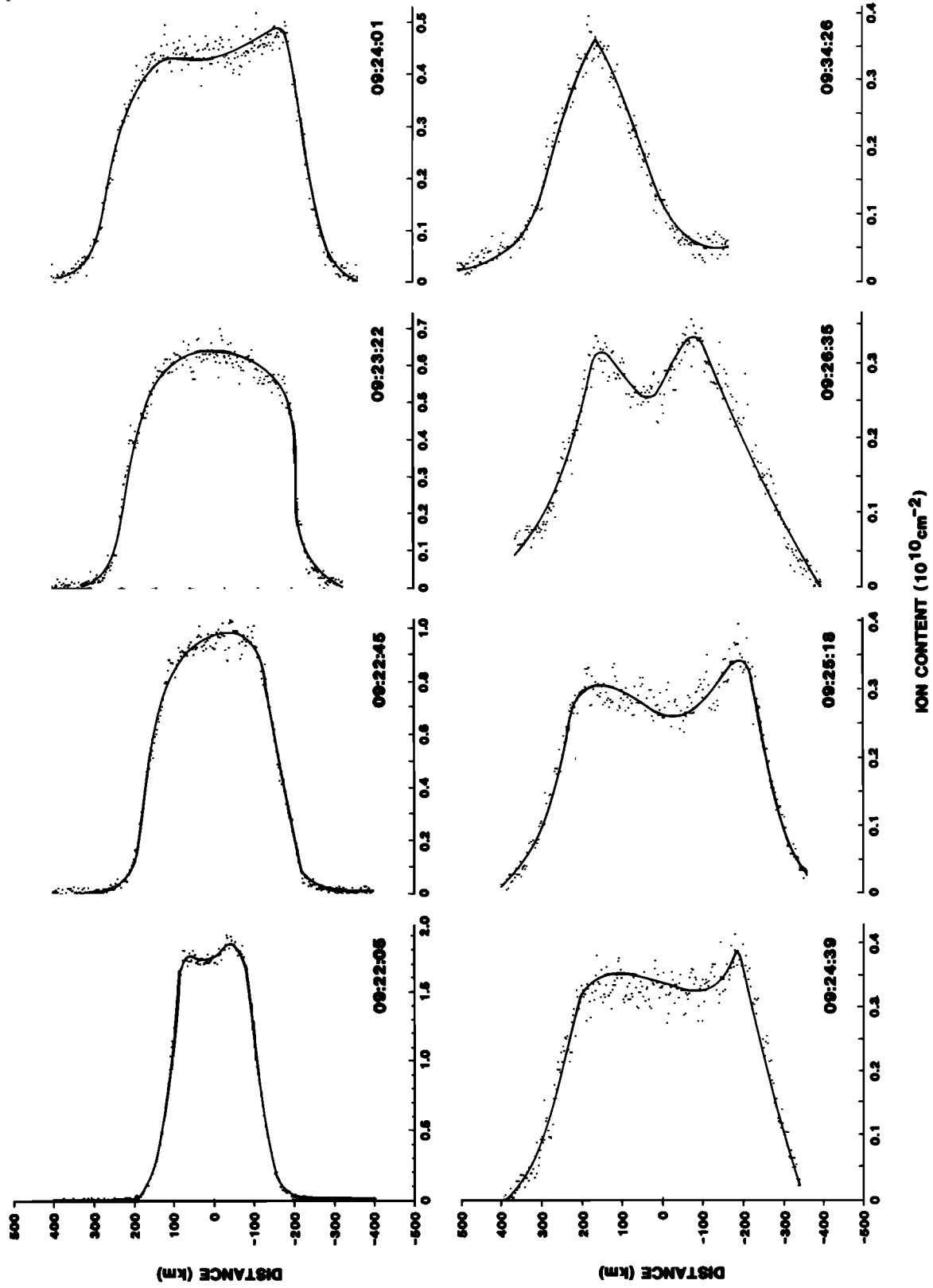
Fig. 9. Profiles of barium ion content obtained from Ortho CCD images of the March 21, 1985, barium release.

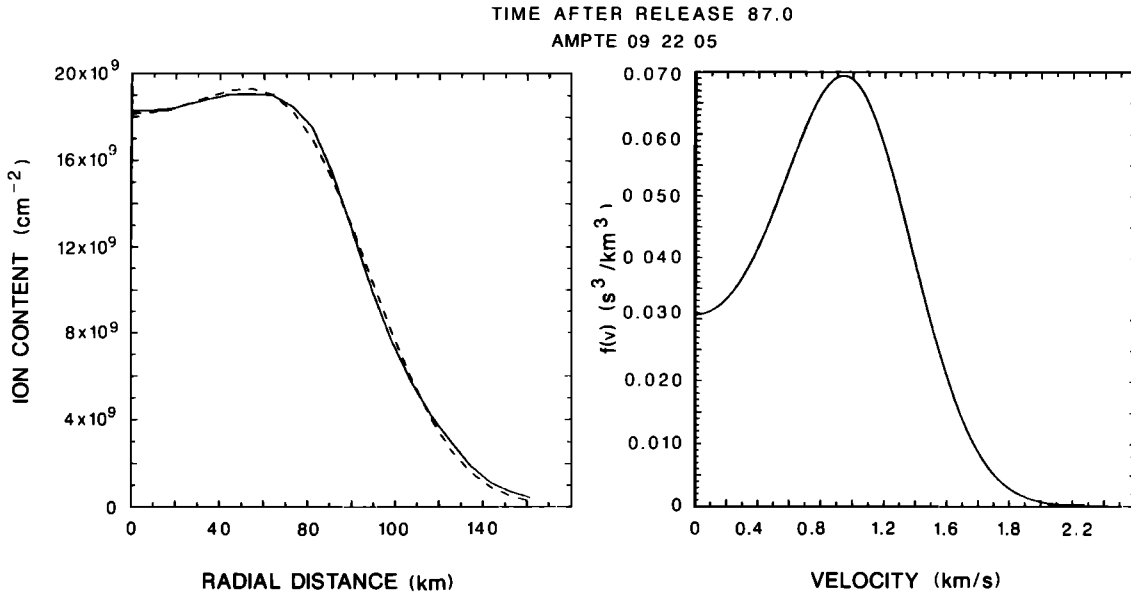TIME AFTER RELEASE 87.0
AMPTE 09 22 05

Fig. 10. Ion content and velocity distributions of the AMPTE barium cloud. The solid line is the measurement of ion content based on the intensified CCD images. The dashed line is the ion density one would obtain using the velocity distribution shown on the right.

The magnetic field components $B_r(r, \theta, t)$ and $B_\theta(r, \theta, \phi, t)$ are zero inside the shell and are given in terms of a magnetic potential

$$B = -\nabla\Phi_m \qquad (3)$$

outside the surface.

First, consider the equations for the magnetic field. Ampère's law in the low-frequency limit is

$$\nabla \times B = \mu_0 j \qquad (4)$$

where j is the current density in the expanding surface. Gauss' theorem applied to $\nabla \cdot B = 0$ yields

$$B \cdot N = -\nabla\Phi_m \cdot N = 0 \qquad (5)$$

where N is the unit normal to the surface. The magnetic potential in the current free regions outside the surface is derived from (3) and (4) with $j = 0$:

$$\nabla^2\Phi_m = 0 \qquad (6)$$

The ambient magnetic field direction is the reference for the spherical polar coordinate system. The potential and components for the undisturbed field are

$$\Phi_{m\infty} = -B_0 r \cos\theta \quad B_{r\infty} = B_0 \cos\theta \quad B_{0\infty} = -B_0 \sin\theta \qquad (7)$$

The magnetic field is found by solving (6) subject to (5) at the cloud surface and to (7) at large distances from the cloud.

The evolution of the plasma surface is described by the equations of continuity and motion:

$$\frac{\partial\rho}{\partial t} + \nabla \cdot (\rho v) = 0 \qquad (8)$$

and

$$\rho \frac{dv}{dt} = j \times B \qquad (9)$$

where $j \times B$ is the surface force due to magnetic pressure and

$$\frac{dv}{dt} = \frac{\partial v}{\partial t} + (v \cdot \nabla)v \qquad (10)$$

Substitution of (2) into (8) gives

$$\left(m\frac{\partial n}{\partial t} + mn\nabla \cdot v + mv \cdot \nabla n\right)\delta$$

$$+ \left[-mn\frac{\partial D}{\partial t} + mnv \cdot \nabla(r - D)\right]\dot{\delta} = 0 \qquad (11)$$

The factors of δ and $\dot{\delta}$ must independently vanish, yielding

$$\frac{\partial D}{\partial t} - v \cdot \nabla(r - D) = 0 \qquad (12)$$

$$\frac{\partial n}{\partial t} + \nabla \cdot (nv) = 0 \qquad (13)$$

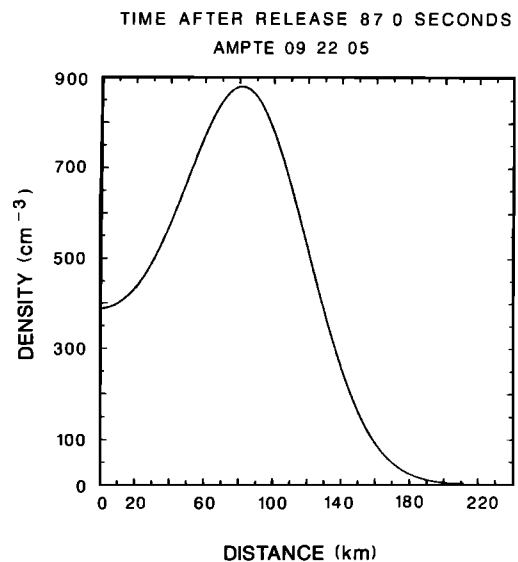TIME AFTER RELEASE 87 0 SECONDS
AMPTE 09 22 05

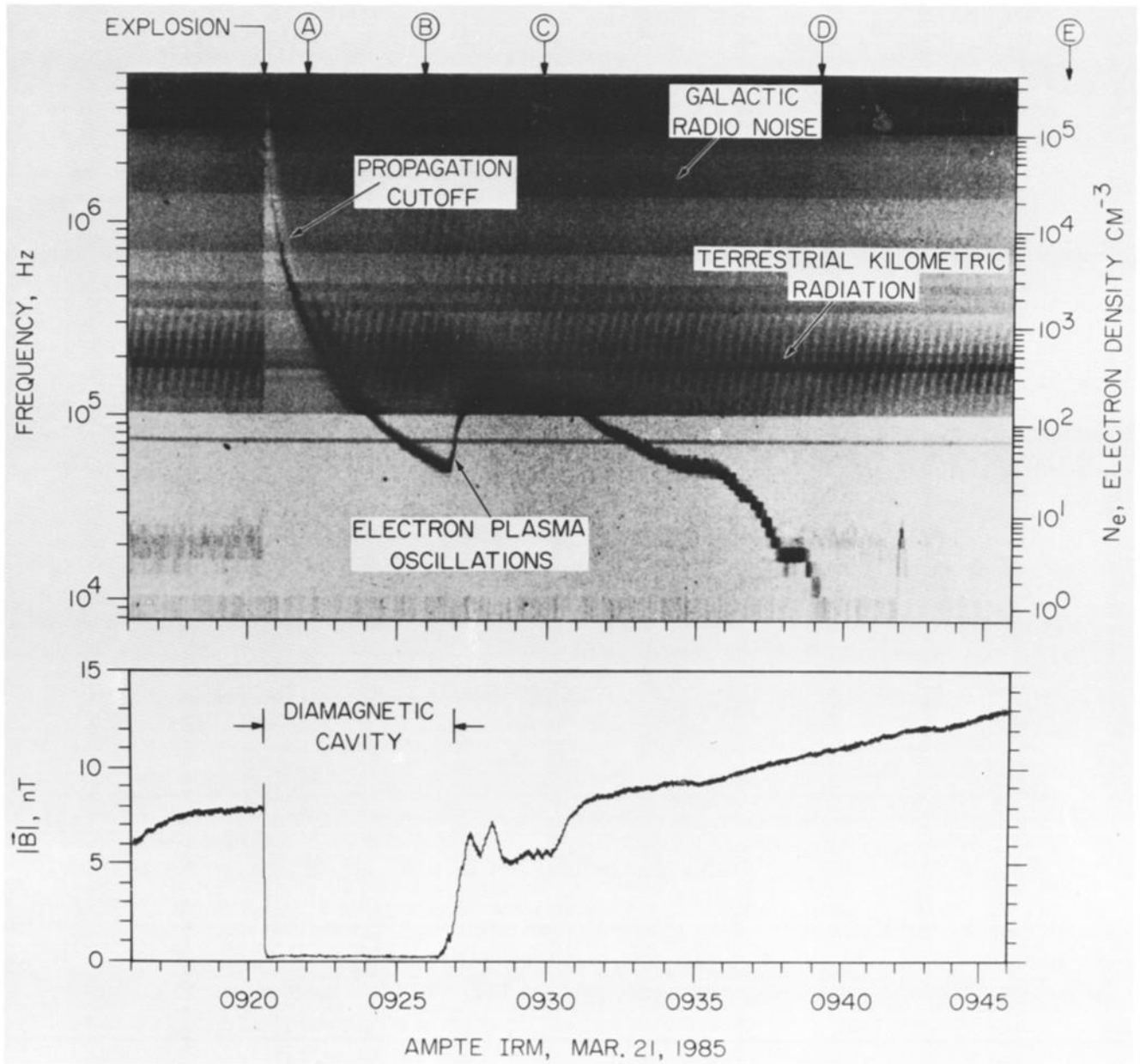Fig. 11. Ion density profile 87 s after the AMPTE barium release.

Fig. 12. Frequency-time spectrogram from the AMPTE IRM. The plasma frequency and propagation cutoff data show effects of the shell-like expansion and of the late-time convection of the cloud relative to the IRM.

The current in the momentum equation (9) is given by (4):

$$\mathbf{j} = \frac{\nabla \times \mathbf{B}}{\mu_0} \qquad (14)$$

Since $\mathbf{B} = 0$ for $r < D$, the $\mathbf{B}$ across the surface is written as a function of the Heaviside unit step function

$$\mathbf{B} = \mathbf{B}^+ H[r - D(\theta, \phi, t)] \qquad (15)$$

where

$$H(x) = 0 \qquad x < 0$$

$$H(x) = \tfrac{1}{2} \qquad x = 0$$

$$H(x) = 1 \qquad x > 0$$

and $\mathbf{B}^+ = \nabla \Phi_m$. Combining (14) and (15) gives

$$\mathbf{j} = \frac{\nabla H[r - D(\theta, \phi, t)] \times \mathbf{B}}{\mu_0}$$

$$= \left[\nabla(r - D) \times \frac{\mathbf{B}}{2} \right] \delta(r - D) \qquad (16)$$

The current from (16) and the mass density from (2) are substituted in (9) to yield the equation of motion:

$$\frac{\partial \mathbf{v}}{\partial t} + (\mathbf{v} \cdot \nabla)\mathbf{v} = \frac{-B^2}{2\mu_0 nm} \nabla(r - D) \qquad (17)$$

Equations (12), (13), and (17) describe the shell under the influence of an external magnetic field.

4. STABLE EVOLUTION OF THE CLOUD

The flute mode instabilities of the cloud are eliminated if all azimuthal (ϕ) variations are neglected. These will be added later with linear-perturbation analysis of the cloud.
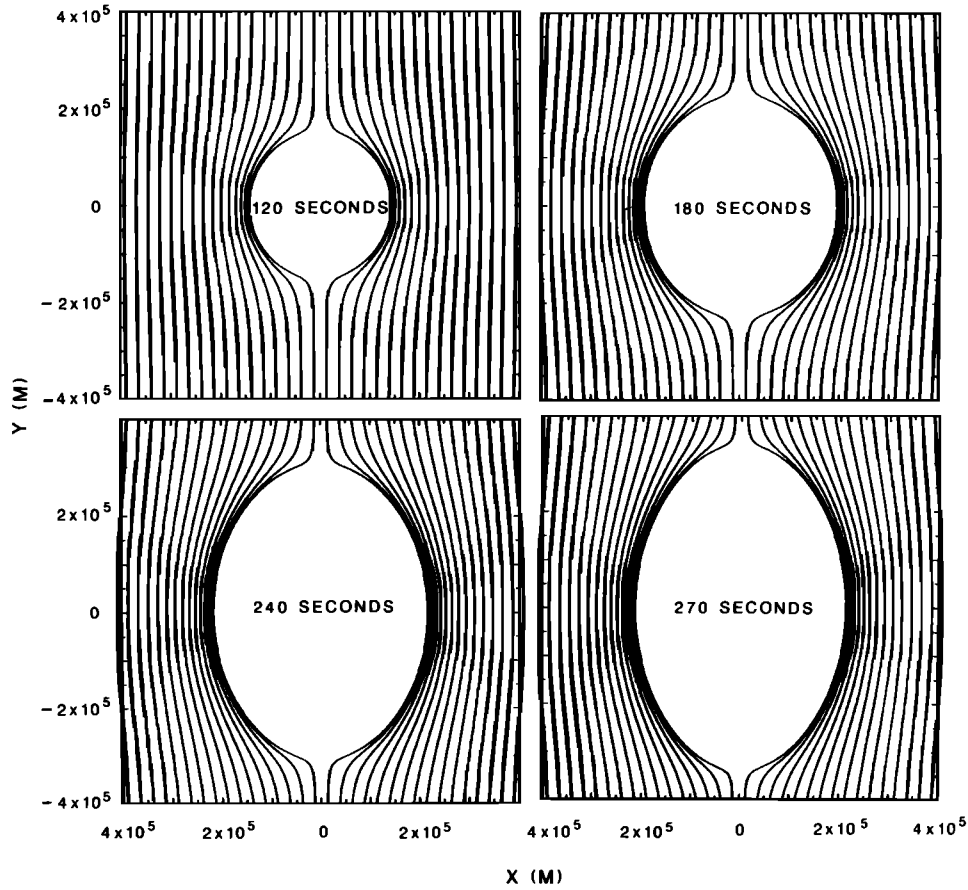
Fig. 13. Compression of the magnetic field lines by the expanding barium shell. The magnetic pressure at the equator of the cloud elongates the cloud and eventually causes its collapse.

With only radial (r) and meridional (θ) variations, the general solution to (6) is written as a series of Legendre polynomials [*Jackson*, 1962]:

$$\phi_m = B_0 r \cos \theta + \sum_l \frac{\alpha_l P_l(\cos \theta)}{r^{(l+1)}} \qquad (18)$$

where α_l are unknowns and $\phi_m \to \phi_{m\infty}$ as $r \to \infty$. The unit normal to the surface $r = D(\theta)$ is

$$N = \frac{D(\theta)\mathbf{r} - D'(\theta)\boldsymbol{\theta}}{(D^2 + D'^2)^{1/2}} \qquad (19)$$

where $\mathbf{r}$ and $\boldsymbol{\theta}$ are unit normal vectors in the radial and meridional directions, respectively. In spherical coordinates, (5) becomes

$$\frac{\partial \phi_m}{\partial r} D(\theta) - \frac{1}{r} \frac{\partial \phi_m}{\partial \theta} \frac{\partial D(\theta)}{\partial \theta} = 0 \qquad (20)$$

Substitution of (18) into (20) at the surface $r = D(\theta)$ yields the equation

$$\sum_{l=0}^{\infty} \alpha_l H_l(x) = F(x) \qquad (21)$$

where

$$x = \cos \theta \qquad F(x) = -B_0[G(x)x - G'(x)(1 - x^2)]$$

$$H_l(x) = G(x)^{-(l+2)}\{[G(x)(l+1) - G'(x)lx]P_l(x) + lP_{l-1}(x)G'(x)\}$$

$$D(\theta) = G(\cos \theta) = G(x)$$

The coefficients α_l with even indices must be zero because of the symmetry of the surface around $x = 0$ ($\theta = \pi/2$). At this point, $G'(0) = 0$ and $F(0) = 0$. For even values of l, $P_l(0) \neq 0$. Consequently, each α_{2m} ($m = 0, 1, 2, \cdots$) must vanish for arbitrary $G(x)$.

Equation (21) is solved by sampling x at points x_i ($i = 1, 2, 3, \cdots$) around the surface. The finite set of linear equations for α_l is

$$\sum_{l=\text{odd}} \alpha_l H_l(x_i) = F(x_i) \qquad (22)$$

$$i = 1, 2, 3, \cdots, N \qquad l = 1, 3, 5, \cdots, 2N - 1$$

With ϕ variations eliminated, (12) and (13) become

$$\frac{\partial D(\theta, t)}{\partial t} = v_r - \frac{\partial D}{\partial \theta} \frac{v_\theta}{D} \qquad (23)$$

$$\frac{\partial n(\theta, t)}{\partial t} = -\frac{n}{D}(2v_r + \cot \theta v_\theta) - \frac{1}{D} \frac{\partial(nv_\theta)}{\partial \theta} + \frac{nv_\theta}{D^2} \frac{\partial D}{\partial \theta} \qquad (24)$$

Similarly, (17) becomes

$$\frac{\partial v_r}{\partial t} + \frac{v_\theta}{D} \frac{\partial v_r}{\partial \theta} - \frac{v_\theta^2}{D} = \frac{-B^2}{2mn\mu_0} \qquad (25)$$

$$\frac{\partial v_\theta}{\partial t} + \frac{v_\theta}{D} \frac{\partial v_\theta}{\partial \theta} + \frac{v_\theta v_r}{D} = \frac{B^2}{2mn\mu_0} \frac{D'}{D} \qquad (26)$$

where $D' = \partial D(\theta, t)/\partial \theta$.

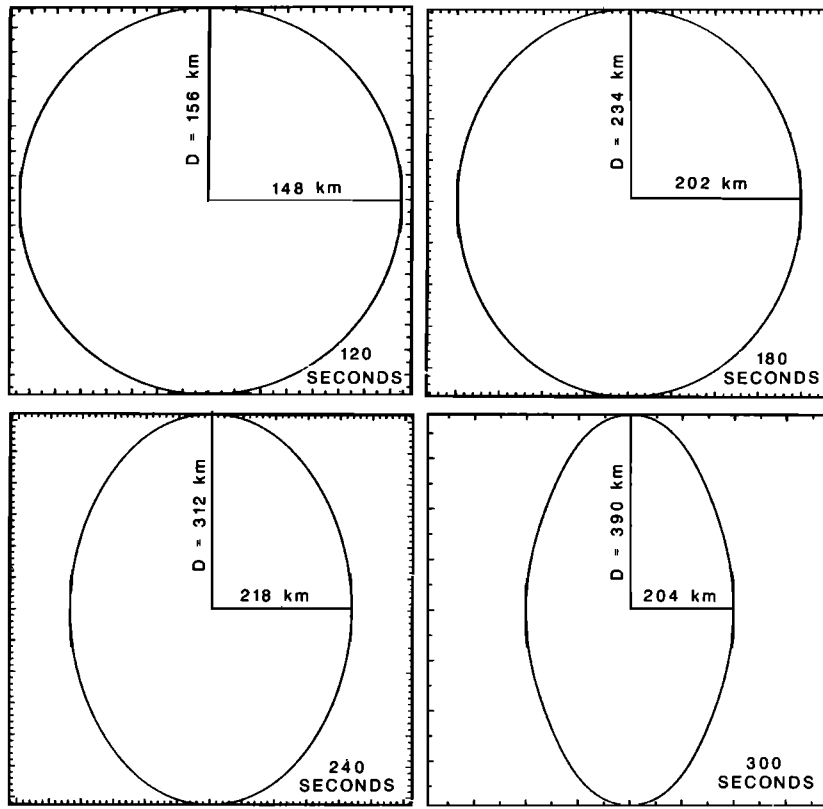Equations (22), (23), (24), (25), and (26) are solved simultaneously with the initial conditions

Fig. 14. Nonspherical expansion of the AMPTE barium cloud.

$$\rho_0 = mn_0(r - r_0) \qquad D_0(\theta, t_0) = r_0 = v_0 t_0$$

$$n_0 = N_0/4\pi r_0^2 \qquad v_{r0} = v_0 \qquad v_{\theta 0} = 0 \qquad (27)$$

$$\phi_{m0} = B_0 \cos\theta\left(\frac{r_0^3}{2r^2} + r\right) \qquad r \geq r_0$$

where subscript 0 refers to the initial condition at t_0 and ϕ_{m0} is the solution to (20) for a spherical surface of radius r_0.

The fluid equations will be examined for energy conservation. Temporarily, assume no meridional variations (i.e., $\partial/\partial\theta = 0$) and constant B field at the surface (i.e., $B = B_0$). Equations (23), (24), and (25) simplify to

$$\frac{\partial D}{\partial t} = v_r \qquad D(0) = r_0 \qquad (28)$$

$$\frac{\partial n}{\partial t} = \frac{-2n}{D} v_r \qquad n(0) = \frac{N_0}{4\pi r_0^2} \qquad (29)$$

$$\frac{\partial v_r}{\partial t} = -\frac{B_0^2}{2mn\mu_0} \qquad v_r(0) = v_0 \qquad (30)$$

Elimination of v_r between (28) and (29) and solving yields

$$n = \frac{N_0}{4\pi D^2} \qquad (31)$$

Substitution for n in (30) yields

$$\frac{\partial v_r}{\partial t} = \frac{-B_0^2}{2m\mu_0} \frac{4\pi D^2}{N_0} \qquad (32)$$

Substitution of v_r in (28) into (32) gives

$$\frac{\partial^2 D}{\partial t^2} = \frac{-B_0^2}{2m\mu_0} \frac{4\pi D^2}{N_0} \qquad (33)$$

Equation (33) is reduced to first order by using

$$\frac{\partial^2 D}{\partial t^2} = \frac{1}{2} \frac{\partial}{\partial D}\left[\left(\frac{\partial D}{\partial t}\right)^2\right] = \frac{-B_0^2 4\pi}{2m\mu_0 N_0} D^2 \qquad (34)$$

with the initial condition $\partial D(0)/\partial t = v_0$. The result

$$\left(\frac{\partial D}{\partial t}\right)^2 = v_0^2 - \frac{B_0^2}{\mu_0} \frac{4\pi D^3}{3} \frac{1}{mN_0} \qquad (35)$$

is set to zero when the cloud reaches steady state at its maximum radial extent. At this time,

$$\tfrac{1}{2}v_0^2 N_0 m = \frac{B_0^2}{2\mu_0} \frac{4\pi D^3}{3} \qquad (36)$$

All of the initial kinetic energy of the cloud particles has been converted into magnetic field energy. The amount of magnetic energy is the unperturbed magnetic field energy density multiplied by displacement volume of the cloud. With this check on validity, the fluid equations may be used with confidence.

The current density at the surface of the cloud is computed from Ampère's law (equation (4)), yielding

$$j_\phi = \left(\frac{B_\theta + D^2 B_r/D}{2\mu_0}\right)\delta[r - D(\theta)] \qquad (37)$$

The current density integrated radially across the surface is

$$J_\phi = \int j_\phi \, dr = \frac{B_\theta + D'B_r/D}{2\mu_0} \qquad (38)$$

where B_ϕ and B_r are evaluated at the surface.

The electric field across the surface is estimated by assuming that the azimuthal current j_ϕ is produced by $\mathbf{E} \times \mathbf{B}$ drift of the electrons:
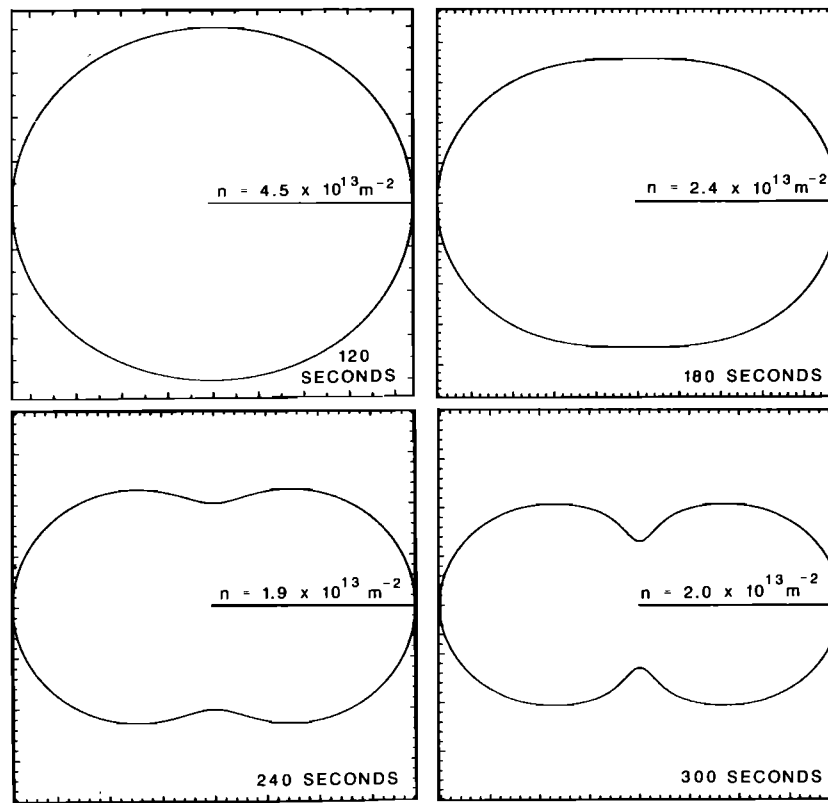
Fig. 15. Polar plots of the ion number density, integrated radially across the cloud surface.

$$j = -en_e v_e = -en_e E \times B/B^2 \qquad (39)$$

Substitution of (16) for j and using $n_e = n(\theta, t)\delta[r - D(\theta, t)]$ gives

$$E = \frac{-B^2}{2en\mu_0}\left[r - \frac{1}{D}\frac{\partial D}{\partial\theta}\theta\right] \qquad (40)$$

The electric field is normal to the expanding surface, pointing inward.

5. SIMULATION OF THE STABLE CLOUD

Using the formulation of the previous section, the stable evolution of the March 31, 1985, AMPTE release is simulated. Figure 13 illustrates the perturbed magnetic field lines. Polar plots of the cloud surface are shown in Figure 14. The expansion perpendicular to the field lines is inhibited by the magnetic pressure. The expansion along the field line is uninhibited. Consequently, the initial, spherical cloud becomes elongated in the direction of the unperturbed magnetic field. The size and time when the cloud reaches its maximum radius are in agreement with the observations.

As the cloud expands, the integrated number density decreases. Figure 15 is a polar plot of n as a function of θ. Initially, the density is uniformly distributed around the surface of the cloud. The density in the direction of the magnetic field lines becomes less than the density at the sides of the cloud. The maximum integrated density is labeled in each plot of Figure 15.

Polar plots of radial velocity are illustrated in Figure 16. The velocity along the magnetic field lines maintains a value of 1300 m/s throughout the expansion. Deceleration due to

the magnetic pressure at the side of the cavity causes the radial velocity for $\theta = \pi/2$ to decrease, reaching zero at 240 s after the release. Past this time, the cavity is collapsing as indicated by the negative radial velocity at 300 s in Figure 16.

A representative polar plot of the meridional velocity V_θ is illustrated in Figure 17 for 180 s after the release. At this time the peak azimuthal speed is 160 m/s.

The magnetic pressure is proportional to B^2. A polar plot of B^2 at equilibrium in the expansion is graphed in Figure 17. As the cloud elongates, the magnetic pressure decreases and has a wider angular spread along the surface of the cloud. The magnetic pressure along the long axis of the cloud is identically zero.

The azimuthal current J_ϕ is shown by the polar plot in Figure 17. The maximum integrated current density required to exclude the magnetic field from the cavity is of the order of 25×10^{-24} A/m. The azimuthal current is maximized at the equatorial ($\theta = \pi/2$) region of the ion cloud.

The spatial distribution of the electric field is shown at the cloud surface by the polar plot in Figure 17. For the first 240 s after release, the maximum electric field is located off the equator. At 240 s after release, the maximum electric field is 15 μV/m. The electric field vector is normal to the surfaces illustrated in Figure 14, pointing inward.

The simulation provides a good description of the March 21 and May 13 diamagnetic cavities. The maximum cloud radius obtained from theoretical calculations is slightly larger than that obtained from the optical data (Table 3). The computed time when the maximum is reached is in agreement with the observations. The uncertainties in the calculations are mainly the input parameters (number of molecules released, expansion velocity, etc.). Slight modification of input parameters could bring the theory and observation in exact agreement.
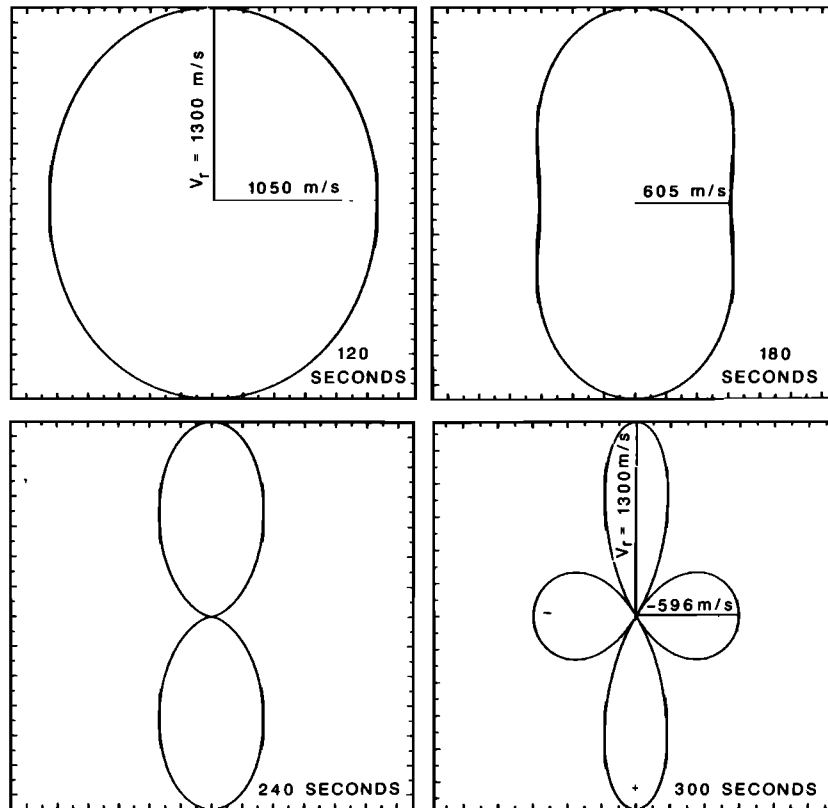
Fig. 16. Polar plots of the radial velocity of the cloud's surface.

6. Unstable Evolution of the Ion Cloud

Both releases of barium into the magnetotail produced a diamagnetic cavity with structured surfaces. Figure 18 illustrates that the scale size of the irregularities is much less than the ion Larmor radius. This scale size, however, is larger than the electron Larmor radius.

The irregularities may be of fluid origin. Fluid interchange instabilities may be examined by inserting small perturbations into the fluid model described in section 3. The fluctuations in cloud surface position, surface density, velocity, and magnetic field are assumed to be small field-aligned perturbations. The variables are written as

$$A(r, \theta, \phi, t) = A_0(r, \theta, t) + A_1(r, \theta, \phi, t) \tag{41}$$

where $A_1 \ll A_0$ and A can represent D, n, v_r, v_θ, v_ϕ, or B.

The stability at the equator ($\phi = \pi/2$) of the cloud is examined with linearized forms of (12), (13), and (17):

$$\frac{\partial D_1}{\partial t} - \mathbf{v}_1 \cdot \nabla(r - D_0) + \mathbf{v}_0 \cdot \nabla D_1 = 0 \tag{42}$$

$$\frac{\partial n_1}{\partial t} + \nabla \cdot (n_0 \mathbf{v}_1) + \nabla \cdot (n_1 \mathbf{v}_0) = 0 \tag{43}$$

$$\frac{\partial \mathbf{v}_1}{\partial t} = (\mathbf{v}_1 \cdot \nabla)\mathbf{v}_0 + (v_0 \cdot \nabla)\mathbf{v}_1 = \frac{B_0{}^2}{2\mu_0 n_0 m} \nabla(D_1)$$
$$+ \frac{B_0{}^2}{2\mu_0 n_0 m} \left(\frac{n_1}{n_0} - \frac{2B_1}{B_0}\right)\nabla(r - D_0) \tag{44}$$

The magnetic field is perpendicular to the unit normal at the surface. The direction of the magnetic field will vary as the cloud surface elongates. The magnitude of the field perturbation is given by $B_1 = -B_0 D_1 f/D_0$, where f is a factor less

than or of the order of unity, which depends on the meridional plane cross section of the shell [see Longmire, 1967; equation 11-9]. At the equator, all derivatives with respect to θ are zero.

Equations (42), (43), and (44) simplify to

$$\frac{\partial D_1}{\partial t} - v_{r1} + \frac{\partial D_1}{\partial \phi} \frac{v_{\phi 0}}{D_0} = 0 \tag{45}$$

$$\frac{\partial n_1}{\partial t} + n_0\left[\frac{2}{D_0} v_{r1} - \frac{2D_1}{D_0{}^2} v_{r0} + \frac{1}{D_0} \frac{\partial v_{\phi 1}}{\partial \phi}\right] + \frac{v_{r0}}{D_0} \frac{\partial n_1}{\partial \phi} = 0 \tag{46}$$

$$\frac{\partial v_{r1}}{\partial t} - \frac{B_0{}^2}{2\mu_0 n_0 m}\left(\frac{n_1}{n_0} + \frac{2fD_1}{D_0}\right) \tag{47}$$

$$\frac{\partial v_{\phi 1}}{\partial t} - \frac{B_0{}^2}{2\mu_0 D_0 n_0 m} \frac{\partial D_1}{\partial \phi} = 0 \tag{48}$$

Further simplification is achieved by using $v_{\phi 0} = 0$ because the azimuthal fluid drift from the electron current is negligible and by using $v_{r0} = 0$ when the cloud has expanded to its maximum extent. A characteristic frequency is defined as

$$\omega_1{}^2 \equiv \frac{B_0{}^2}{2\mu_0 D_0 n_0 m} \tag{49}$$

Assuming a shell thickness τ_0 allows the mass density to be defined as $\rho_0 = n_1 m/\tau_0$. The characteristic frequency becomes

$$\omega_1{}^2 = \frac{B_0{}^2}{2\mu_0 \rho_0 D_0 \tau_0} = \frac{v_A{}^2}{2D_0 \tau_0} \tag{50}$$

where v_A is the Alfvén velocity.

The ϕ and t variations of the perturbations are assumed to vary as $e^{i(\omega t - M\phi)}$ where M is the number of field-aligned irregularities around the equator of the cloud. With these assumptions, (45)–(48) become
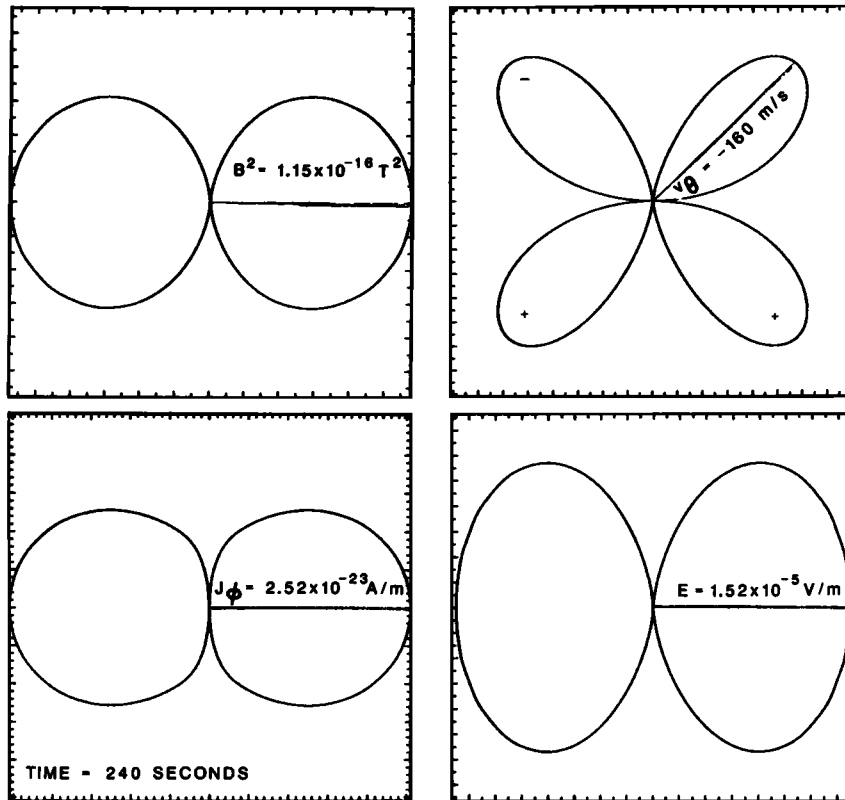
Fig. 17. Polar plot of (upper left) square of the magnetic field strength, (upper right) meridional velocity, (lower left) radially integrated current density, and (lower right) electric field normal to the cloud surface. The electric field generates the azimuthal current required to exclude the magnetic field from the cavity.

$$i\omega D_1 - v_{r1} = 0 \tag{51}$$

$$i\omega n_1 + \frac{2n_0}{D_0} v_{r1} + \frac{n_0}{D_0} (-iM)v_{\phi 1} = 0 \tag{52}$$

$$i\omega v_{r1} - \omega_1{}^2 D_0\left(\frac{n_1}{n_0} + \frac{2fD_1}{D_0}\right) = 0 \tag{53}$$

$$i\omega v_{\phi 1} - \omega_1{}^2(-iM)D_1 = 0 \tag{54}$$

which yields the dispersion equation

$$\omega^2[\omega^2 - 2\omega_1{}^2(1 - f)] = M^2\omega_1{}^4 \tag{55}$$

This equation has four roots. The complex frequency $\omega = \omega_r + i\gamma$ where γ is the instability growth rate. For $M \gg 1$, one of the roots yields

$$\omega_r = 0 \tag{56}$$

$$\gamma = \omega_1 M^{1/2} \tag{57}$$

The instability is driven by the magnetic field pressure.

The AMPTE magnetotail release on March 21, 1985, produced flute mode irregularities with $M = 24$. The characteristic frequency ω_1 is equal to 8×10^{-3} rad/s. The growth rate
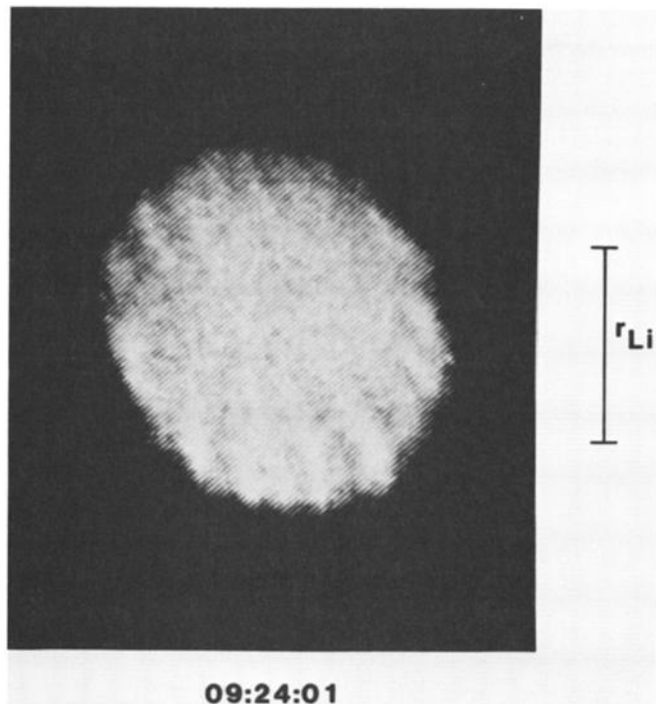

TABLE 3. Comparison of Measurements and Computations

	Release Date	
	March 21	May 13
Maximum radius, km		
Measured	210	105
Calculated	218	130
Time for start of collapse, s		
Measured	230	150
Calculated	240	142

09:24:01

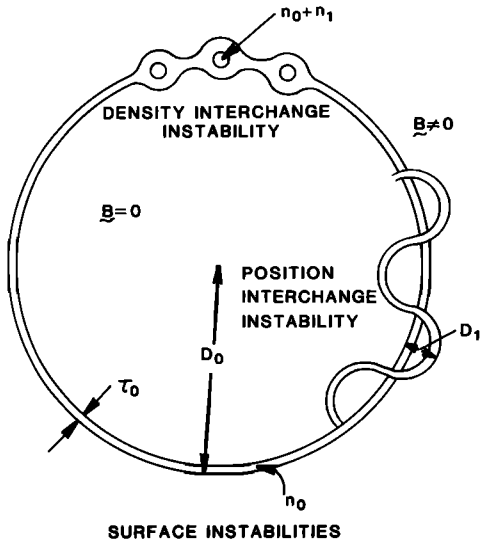Fig. 18. CCD image showing irregularities on the surface of the barium ion cloud.

Fig. 19. Interchange instabilities which can ripple the cloud surface.

for the AMPTE release is $\gamma = 3.9 \times 10^{-2}$ s^{-1}, yielding a growth time of 26 s.

A schematic drawing of fluid irregularities on the cloud surface is shown in Figure 19. Fluctuations in D are a position interchange instability. Variations in n represent a density interchange instability. The optical observations illustrated in Figures 5 and 18 favor this latter effect.

This fluid instability is driven by the magnetic pressure on the surface. Using (51) and (53), the relationship between surface position and surface density of the growing instability is given by

$$\frac{n_1}{n_0} = M \frac{D_1}{D_0} \qquad (58)$$

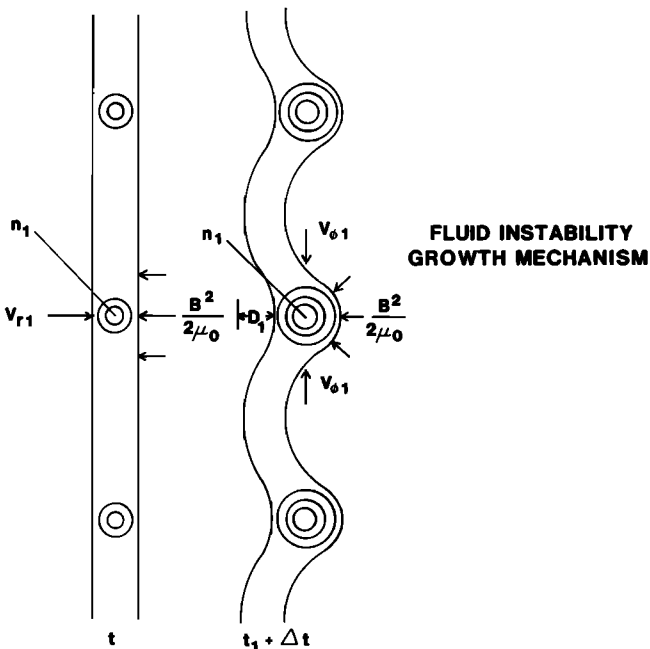Since $M \gg 1$, the normalized density fluctuations are much

larger than the normalized position fluctuations. This is consistent with the optical observations.

The physical process for the instabilities is illustrated in Figure 20. An enhancement in surface density n_1 produces an increase in radial velocity (v_{r1}). The surface erupts out a distance D_1. The magnetic pressure acts perpendicular to the surface to increase $v_{\phi1}$, squeezing the eruption. This causes the surface density to further enhance and leads to the instability growth. This process works if the distance between irregularities is greater than or equal to the layer thickness.

The theory is limited by the assumption of an infinitely thin plasma shell. Actually, the shell has a finite thickness τ_0. For $\tau_0 \rightarrow 0$ the growth rate $\gamma = \omega_1 M^{1/2}$ increases without limit as $M \rightarrow \infty$. From the observations we find that the scale size of the irregularities around the equator is equal to the thickness of the cloud. Consequently, the appropriate number of irregularities around the equator is $M = 2\pi D_0/\tau_0$ for a finite thickness cloud. The growth rate for the instability becomes

$$\gamma = \omega_1 M^{1/2} = \frac{v_A \pi^{1/2}}{\tau_0} \qquad (59)$$

The growth time $(= 1/\gamma)$ is approximately the time for an Alfvén wave to transit the cloud thickness.

The electrons and ions inside the diamagnetic cavity catch up to the cloud surface as it decelerates. The surface thickness becomes reduced as the cavity approaches equilibrium. The

AMPTE DIAMAGNETIC CAVITY IN THE MAGNETOTAIL

$\omega_{ci} = 5.2 \times 10^{-3}$ s^{-1} $r_{Li} = 2.3 \times 10^5$ m

$\omega_{ce} = 1.3 \times 10^3$ s^{-1} $r_{Le} = 460$ m

LOWER HYBRID DRIFT INSTABILITY $\mathbf{k} \cdot \mathbf{B_0} = 0$

$\omega_{Lh} = (\omega_{ce} \omega_{ci})^{1/2} = 2.6$ s^{-1}

$\omega_{ci} \ll \gamma_m \simeq \omega_{Lh} \ll \omega_{ce}$ $\tau_m \simeq 0.4$ S   UNMAGNETIZED IONS

$(r_{Li})^{-1} \ll k_m \simeq (r_{Le})^{-1}$ $\lambda_m \simeq 3$ km   MAGNETIZED ELECTRONS

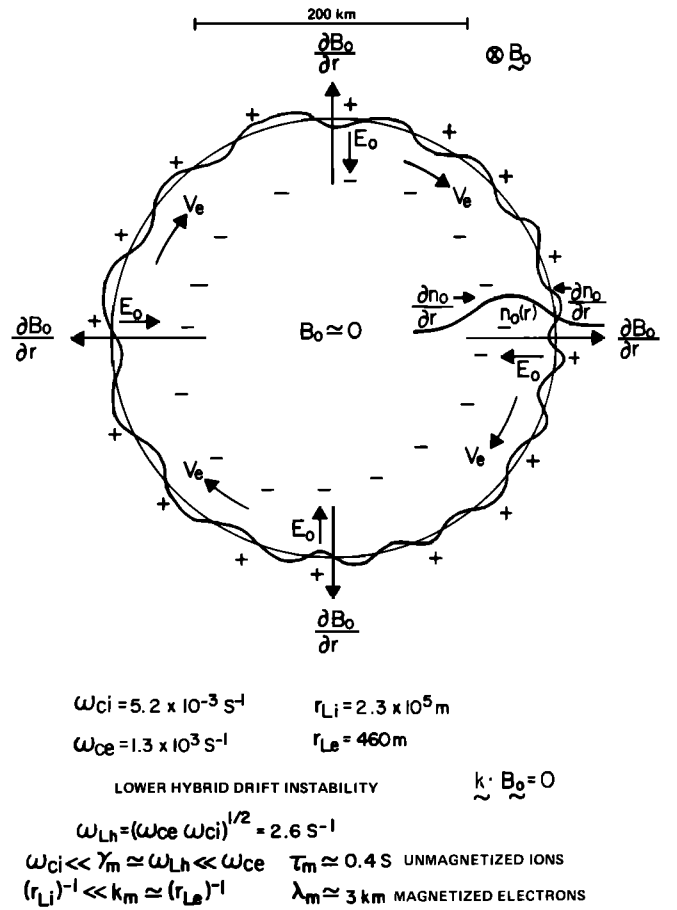Fig. 20. Eruptions from the surface of the cloud enhanced by the magnetic field pressure.

Fig. 21. Lower hybrid drift instability mechanism for production of irregularities.

surface layer thickness is limited to one gyrodiameter. The gyroradius of the electron orbit is given by

$$r_{Le} = \frac{v_e}{\Omega_{ce}} \tag{60}$$

Quasi-neutrality between electrons and ions will cause the barium ions to fill out the region populated by the electron gas [Dum, 1984].

The electron velocity is determined by the equilibrium between plasma pressure and magnetic field pressure at the cloud surface. The plasma β is unity, i.e.,

$$\beta = \frac{m_e n_e v_e^2/2}{B^2/2\mu_0} = 1 \tag{61}$$

Solving for electron velocity yields

$$v_e = \frac{B}{(\mu_0 m_e n_e)^{1/2}} = \frac{c\Omega_{ce}}{\omega_{pe}} \tag{62}$$

where ω_{pe} is the electron plasma frequency.

The electron gyroradius becomes

$$r_{Le} = \frac{v_e}{\Omega_{ce}} = \frac{c}{\omega_{pe}} \tag{63}$$

The minimum thickness of the cloud surface is $\tau_0 = 2r_{Le} = 2c/\omega_{pe}$. Substitution for the growth rate (equation (57)) yields

$$\gamma \simeq v_A/r_{Le} = v_A \omega_{pe}/c \simeq (\Omega_{ce}\Omega_{ci})^{1/2} \tag{64}$$

This is the growth rate for the LHD instability.

Conditions for the LHD instability are illustrated in Figure 21 for the equatorial cross section of the AMPTE cloud. Radially outward gradients in magnetic field strength and in plasma density are required. An azimuthal electron drift given as an E × B drift driven by a polarization electric field and/or as a diamagnetic drift is also required. Flute mode irregularities form around the surface. Further details of this instability are found in the paper by Davidson et al. [1977].

The LHD instability has been used to explain flute irregularities in laboratory plasma theta pinches. The AMPTE magnetotail release is analogous to the theta pinch with the magnetic compression replaced by the plasma expansion. The scale size of the irregularities from the LHD instability is

March 21

$$\lambda_{LHD} \simeq 2\pi r_{Le} = 2.3 \times 10^3 \text{ m}$$

May 13

$$\lambda_{LHD} \simeq 2\pi r_{Le} = 1.0 \times 10^3 \text{ m}$$

This scale is about a factor of 10 smaller than the measured scale. Expansion of frozen-in irregularities or preferential growth of longer-wavelength irregularities may explain this discrepancy.

7. DISCUSSION

The MHD model of the AMPTE barium ion release in the magnetotail provides good agreement with the observations.

The primary limitation of the model is the inherent supposition that the barium ion shell is infinitely thin. This supposition allows us to ignore the physical processes that determine the thickness of the shell. Such processes include (1) penetration of the magnetic field across the surface, (2) finite ion and electron temperatures, (3) distributed polarization electric fields and electron currents across the surface, and (4) finite resistivity due to wave-particle instabilities.

We have also neglected the coupling of the barium ions with the background plasma. The magnetized protons displaced by expanding barium ion clouds represent a small fraction (0.1%) of the injected ion mass. Consequently, mass loading of the cloud surface can be neglected. The high-temperature background plasma may play an important role in forming the diffuse halo around the dense core of barium ions.

REFERENCES

Carlsten, J. L., Photoionization of barium clouds via the ^3D metastable levels, *Planet. Space Sci.*, 23, 53, 1975.

Davidson, R. C., N. T. Gladd, C. S. Wu, and J. D. Huba, Effects of plasma beta on the lower-hybrid-drift instability, *Phys. Fluids*, 20, 301, 1977.

Dum, C. T., AMPTE: Diamagnetic effect and anomalous transport in expanding plasma clouds, *AMPTE Sci. Preprint 08*, Max-Planck-Inst. für Phys. und Astrophys., Garching, Federal Republic of Germany, March 1984.

Gurnett, D. A., R. R. Anderson, P. A. Bernhardt, H. Lühr, G. Haerendel, O. H. Bauer, H. C. Koons, and R. H. Holzworth, Plasma waves associated with the first AMPTE magnetotail barium release, *Geophys. Res. Lett.*, 13, 644, 1986.

Horak, H. C., and R. W. Whitaker, Resonance fluorescence in barium ion clouds, *Planet. Space Sci.*, 30, 897, 1982.

Jackson, J. D., *Classical Electrodynamics*, p. 56, John Wiley, New York, 1962.

Longmire, C. L., *Elementary Plasma Physics*, pp. 241–249, Wiley Interscience, New York, 1967.

Lühr, H., N. Klöcker, and A. H. Acuña, The diamagnetic effect during AMPTE's tail releases, *Adv. Space Res.*, in press, 1986.

R. R. Anderson and D. A. Gurnett, Department of Physics and Astronomy, University of Iowa, Iowa City, IA 52242.

P. A. Bernhardt, M. B. Pongratz, and R. A. Roussel-Dupre, Los Alamos National Laboratory, Code ESS-7, MS D466, Los Alamos, NM 87545.

G. Haerendel and A. Valenzuela, Max-Planck-Institut für Physik und Astrophysik, 8046 Garching bei München, Federal Republic of Germany.